How to cite: *Angew. Chem. Int. Ed.* **2022,** *61,* e202213015
International Edition: doi.org/10.1002/anie.202213015
German Edition: doi.org/10.1002/ange.202213015

Gas Separation

Boosting Ethane/Ethylene Separation by MOFs through the Amino-Functionalization of Pores

Gang-Ding Wang, Rajamani Krishna, Yong-Zhi Li, Wen-Juan Shi, Lei Hou, Yao-Yu Wang, and Zhonghua Zhu*

Abstract: Adsorption technology based on ethane-selective materials is a promising alternative to energy-intensive cryogenic distillation for separating ethane (C_2H_6) and ethylene (C_2H_4). We employed a pore engineering strategy to tune the pore environment of a metal–organic framework (MOF) through organic functional groups and boosted the C_2H_6/C_2H_4 separation of the MOF. Introduction of amino ($-NH_2$) groups into Tb-MOF-76 not only decreased pore sizes but also facilitated multiple guest-host interactions in confined pores. The NH_2-functionalized Tb-MOF-76(NH_2) has increased C_2H_6 and C_2H_4 uptakes and C_2H_6/C_2H_4 selectivity. The results of experimental and simulated transient breakthroughs reveal that Tb-MOF-76(NH_2) has significantly improved one-step separation performance for C_2H_6/C_2H_4 mixtures with a high C_2H_4 (>99.95 %) productivity of 17.66 $L\,kg^{-1}$ compared to 7.53 $L\,kg^{-1}$ by Tb-MOF-76, resulting from the suitable pore confinement and accessible $-NH_2$ groups on pore surfaces.

Introduction

Ethylene (C_2H_4) is the most demanded raw material in the petrochemical industry, with a global production exceeding 210 million tons in 2021. C_2H_4 is mainly produced by the thermal decomposition of ethane (C_2H_6) and steam cracking of fossil fuels, and inevitably contains a certain amount of C_2H_6 residue (5 %–9 %) that must be cut down to guarantee the polymerization utilization of C_2H_4.[1] However, the separation of C_2H_6 and C_2H_4 is extremely challenging because of similar kinetic diameters and boiling points between them (C_2H_6: 4.44 Å, 184.55 K; C_2H_4: 4.16 Å, 169.42 K).[2] Thus far, the well-developed separation of C_2H_4/C_2H_6 has been realized by energy-intensive distillation operated in a large distillation tower at low temperatures and high pressures.[3] Exploiting efficient separation techniques aiming to produce polymer-grade C_2H_4 is highly imperative.[4]

Adsorbent-based separation using porous materials has attracted particular attention for low energy consumption and high efficiency.[5] C_2H_6/C_2H_4 separation can be implemented by C_2H_4-selective or C_2H_6-selective adsorbents. C_2H_4-selective adsorbents preferentially adsorb C_2H_4 over C_2H_6, however, the subsequent desorption process is needed to obtain C_2H_4 product, meanwhile the product is generally of low purity due to C_2H_6 co-adsorption in adsorbents.[6] By comparison, C_2H_6-selective adsorbents that preferentially capture C_2H_6 impurity over C_2H_4 attain one-step harvest of C_2H_4 in single breakthrough operation process.[7] At present, the C_2H_6-selective adsorbents have remained relatively underexplored as installing C_2H_4-binding sites in adsorbents is easier to operate than C_2H_6-binding sites. So the exploitation of excellent C_2H_6-selective adsorbents is the desired pursuit for C_2H_4 purity goal.

Metal-organic frameworks (MOFs) are a new type of porous materials with wide variety of application prospects in many fields, especially the unique of tunable pore environment and easy modification enable them to be ideal platforms for designing C_2H_6-selective adsorbents.[8] These adsorbents require specific recognition for C_2H_6 over C_2H_4 and high uptake for C_2H_6. Hitherto, although some C_2H_6-selective MOFs have been reported,[9] however, the deficiencies, such as low selectivity, unsatisfied capacity, and inferior structural stability are also usually encountered. For instance, creating inert/non-polar pore environment is effective to construct C_2H_6-selective MOFs, however, the materials exhibit relatively low loading for C_2H_6 due to lacking strong C_2H_6-interacting sites.[10] The functionalization of open metal sites (OMSs) through O_2 reported by Chen et al. greatly enhances the C_2H_6 uptakes, yielding a recorded C_2H_6/C_2H_4 selectivity of 4.4, which shows a pioneering work in creating C_2H_6-selective MOFs.[7b] This strategy needs removing the coordinated solvents followed by introducing O_2 molecules to bind the OMSs, and the material is sensitive to air/moisture and must to be handled in a glove box. However, shielding the OMSs by coordinated solvent molecules avoids the metal$\cdots\pi$ interactions between OMSs and C_2H_4, providing an alternative to creating C_2H_6-selective

[*] Dr. G.-D. Wang, Dr. Y.-Z. Li, Dr. W.-J. Shi, Prof. L. Hou, Prof. Y.-Y. Wang
Key Laboratory of Synthetic and Natural Functional Molecule of the Ministry of Education, College of Chemistry & Materials Science, Northwest University
Xi'an, 710127 (P. R. China)
E-mail: lhou2009@nwu.edu.cn

Prof. R. Krishna
Van 't Hoff Institute for Molecular Sciences, University of Amsterdam
1098 XH Amsterdam (The Netherlands)

Prof. Z. Zhu
School of Chemical Engineering, The University of Queensland
Brisbane 4072 (Australia)

MOFs. In addition, there are also other C_2H_6-selective MOFs that mainly rely on synergy in pore-matching effects and multiple interactions between the framework and C_2H_6 with more C–H bonds.[11]

Targeting the development of outstanding separation materials for C_2H_6/C_2H_4 mixtures, isoreticular chemistry allows us through pore engineering strategy to precisely design and regulate the pores of MOFs. The pore environment of C_2H_6-selective MOFs can be tuned by modifying linkers with organic groups, thus it would improve the C_2H_6/C_2H_4 separation potential of MOFs. However, only very rare examples were reported on the study of C_2H_6/C_2H_4 separation by pore engineering strategy in MOFs.[3b,8c,9c,10,11] Amino (–NH_2) group effects on the gas adsorption and separation were well demonstrated by other research groups.[12] For example, using –NH_2 groups or diamine compounds to modify the organic linkers or metal centers in MOFs, the CO_2 adsorption amounts were greatly increased.[12a,e,f] In addition, –NH_2 groups can also serve as accessible sites to form multiple C–H···N hydrogen bonds with light hydrocarbon molecules to enhance the interactions between MOFs and hydrocarbons.[13] However, there are very few comparison studies on the C_2H_6/C_2H_4 mixtures separation between amino-functionalized MOFs and parent MOFs.[8b] So the comparative in-depth study on C_2H_6/C_2H_4 separation properties in the pair of isoreticular MOFs are urgently needed.

With this in mind, we noticed Tb-MOF-76 based on 1,3,5-benzenetricarboxylate (BTC) as a platform due to its analogues of M–MOF-76 (M = Y, Sm, Eu, and Dy) showed the reversed C_2H_6/C_2H_4 adsorption selectivity.[14] According to isoreticular chemistry, isomorphic Tb-MOF-76(NH_2) was readily obtained by using the amino-functionalized linker 2-amino-1,3,5-benzenetricarboxylate (NH_2-BTC), which provides an elegant example of controlling pore chemistry for advancing C_2H_6/C_2H_4 separation. It was found that the introduction of –NH_2 groups decreased pore sizes from 7.9×7.9 Å^2 in Tb-MOF-76 to 7.2×7.2 Å^2 in Tb-MOF-76(NH_2), facilitating the multiple guest-host interactions in confined pores. Through obstructing the OMSs with the water ligands, both MOFs show the C_2H_6-selective adsorption behavior. Compared to Tb-MOF-76, Tb-MOF-76(NH_2) has increased C_2H_4 and C_2H_6 uptakes and C_2H_6/C_2H_4 selectivity (1.7 *vs* 2.1), superior to most reported C_2H_6-selective MOFs, and also displays the improved separation performance for 1/1, 1/9, and 1/15 (v/v) C_2H_6/C_2H_4 mixtures, obtaining the pure C_2H_4 by one step. Thus, the installation of –NH_2 groups optimizes the pore environment elaborately, endowing Tb-MOF-76(NH_2) with great potential as a superior adsorbent for C_2H_4 purification from C_2H_6/C_2H_4 mixtures.

Results and Discussion

In performing functional modification, it is of paramount importance to synthesize MOFs with high stability. Herein, adjustable and highly stable Tb-MOF-76 was selected as a platform for –NH_2 functionalization. The high quality of single crystals of Tb-MOF-76(NH_2) can be prepared through the solvothermal reaction of NH_2-BTC with Tb^{3+} ions, which is isostructural to Tb-MOF-76 crystallized in a $P4_122$ space group (CCDC No. 2192249, as shown in Figure S1–S3, Table S1 and S2).[15] The Tb^{3+} centres have distorted pentagonal-bipyramidal geometries (Figure S4), and are bridged by carboxylates to form a helical rod-shaped secondary building unit (SBU) (Figure 1). The SBUs are connected with organic linkers to construct an open framework possessing square channels. Compared to Tb-MOF-76, Tb-MOF-76(NH_2) has free –NH_2 groups pointing into the channels, which decreases the pore dimensions to 7.2×7.2 Å^2 from 7.9×7.9 Å^2 (excluding the van der Waals radii) in Tb-MOF-76 (Figure 1). The pore sizes of Tb-MOF-76(NH_2) is closer to the kinetic diameter of C_2H_4 (4.16 Å) and C_2H_6 (4.44 Å), which would impose multipoint adsorbing sites for C_2H_4 and C_2H_6 molecules considering size-matching effect.

Thermogravimetric analysis (TGA) showed the removal of coordinated water molecules at a high temperature for the two MOFs (Figure S5 and S6). During activation process of MOFs, the coordinated water molecules were hold in order to avoid the formation of OMSs that on one hand are unfavorable to binding C_2H_6 over C_2H_4, on the other hand are easily attacked by water in realistic work environment. For this regard, the MOFs exchanged in methanol for 72 h were activated at 373 K under high vacuum to remove lattice solvents, as shown in TGA curves (Figure S5 and S6). Power X-ray diffraction (PXRD) of two desolvated MOFs remain unchanged, indicating the framework rigidness (Figure S2 and S3). Both MOFs show typically type-I isotherms for N_2 at 77 K (Figure 2a). As expected, the introduction of –NH_2 groups moderately decreases the pore sizes of Tb-MOF-76(NH_2) (8.2 Å) compared to Tb-MOF-76 (8.8 Å), the smaller pore sizes would be more favorable to form multiple contacts between the framework and gases.

To evaluate the tuning on absorption performance via –NH_2 modification, the sorption isotherms of C_2H_6 and C_2H_4 were measured at 273 and 298 K (Figure 2b and 2c). At 100 kPa, the loadings of Tb-MOF-76 for C_2H_6 and C_2H_4

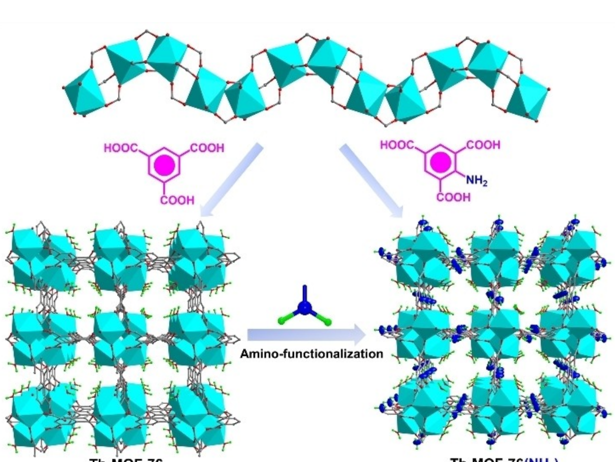

Figure 1. Isostructural frameworks of Tb-MOF-76 and Tb-MOF-76(NH_2) assembled by rod-shaped SBUs and BTC/NH_2-BTC linkers.

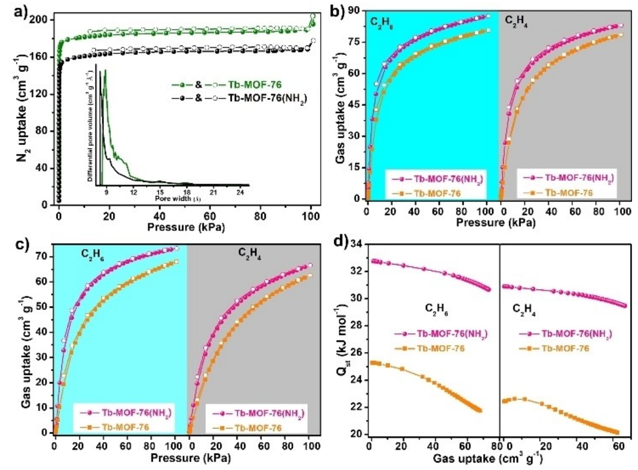

Figure 2. a) N_2 sorption isotherms at 77 K, the insert indicates pore size distribution; b) C_2H_6 and C_2H_4 sorption isotherms at 273 K; c) C_2H_6 and C_2H_4 sorption isotherms at 298 K; d) Q_{st} plots of C_2H_6 and C_2H_4.

are 68.0 and 62.6 $cm^3 g^{-1}$ at 298 K and 80.6 and 78.6 $cm^3 g^{-1}$ at 273 K, respectively, while the loadings of Tb-MOF-76(NH_2) for C_2H_6 and C_2H_4 are increased to 73.3 and 66.6 $cm^3 g^{-1}$ at 298 K and 87.5 and 83.1 $cm^3 g^{-1}$ at 273 K, respectively. Compared to Tb-MOF-76, besides higher uptakes, Tb-MOF-76(NH_2) also exhibited steeper adsorption isotherms of C_2H_6 and C_2H_4, implying the immobilization of $–NH_2$ groups strengthens the adsorbate-adsorbent interactions. This finding coincides with the calculated results of isosteric heat of adsorption (Q_{st}) by fitting the gas adsorption isotherms at 273, 298, and 313 K to the virial equation (Figure 2d, S7–S12), which display notably higher Q_{st} values in two MOFs for C_2H_6 (32.8–30.7 $kJ mol^{-1}$ for Tb-MOF-76(NH_2), 25.2–21.7 $kJ mol^{-1}$ for Tb-MOF-76) compared to C_2H_4 (30.9–29.5 $kJ mol^{-1}$ for Tb-MOF-76(NH_2), 22.4–20.1 $kJ mol^{-1}$ for Tb-MOF-76) in the measured pressure region. Meanwhile, Tb-MOF-76(NH_2) shows higher Q_{st} for the two gases relative to Tb-MOF-76. The decreased pore sizes in Tb-MOF-76(NH_2) allow closer interactions between the framework and gas molecules, improving adsorption affinity. For two MOFs, besides the higher Q_{st} values of C_2H_6 than C_2H_4, the isotherms of C_2H_6 are also increased more sharply than C_2H_4 (Figure S11 and S12). These observations validate the stronger affinity of the framework toward C_2H_6 over C_2H_4, supporting the C_2H_6-selective behavior in two MOFs.

Although the C_2H_6 uptake of Tb-MOF-76(NH_2) at 298 K and 100 kPa is lower than some benchmark C_2H_6-selective MOFs (Figure 3a), such as CPM-233 (166.8 $cm^3 g^{-1}$),[16] CPM-733 (159.6 $cm^3 g^{-1}$),[16] JNU-2 (92 $cm^3 g^{-1}$),[17] and TJT-100 (86 $cm^3 g^{-1}$),[18] but exceeds or is comparable with most reported top-performance adsorbents for C_2H_6/C_2H_4 separation, including Cu(Qc)$_2$ (60 $cm^3 g^{-1}$),[11] MAF-49 (38 $cm^3 g^{-1}$),[13a] NKCOF-23 (60.5 $cm^3 g^{-1}$),[7a] and HIAM-102 (48.3 $cm^3 g^{-1}$).[19] The cycle tests demonstrate the facile reactivation of Tb-MOF-76(NH_2), wherein the sorption isotherms of C_2H_6 and C_2H_4 are reversible and have no decrease in adsorption capacities (Figure 3b).

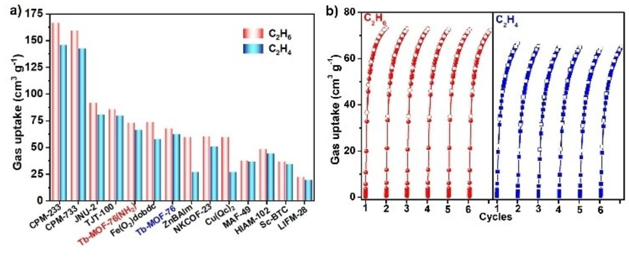

Figure 3. a) Comparison of C_2H_4 and C_2H_6 uptakes in some C_2H_6-selective materials; b) C_2H_6 and C_2H_4 of sorption cycles for Tb-MOF-76(NH_2) at 298 K.

Ideal adsorbed solution theory (IAST) was utilized to assess and compare the selectivity of Tb-MOF-76(NH_2) and Tb-MOF-76 for 1/1, 1/9, and 1/15 C_2H_6/C_2H_4 mixtures at 298 K (Figure S13 and S14). Tb-MOF-76 exhibits the C_2H_6/C_2H_4 selectivity of about 1.7 for these mixtures at 100 kPa, while Tb-MOF-76(NH_2) shows an obviously high selectivity of about 2.1 (Figure 4a). Since the low content of C_2H_6 in actual cracked gas mixtures (C_2H_6/C_2H_4, 1:15), it is crucial that the material has a high loading for C_2H_6 at low partial pressure. Figure 4b presents a comparison of Tb-MOF-76(NH_2) with some typical C_2H_6-selective MOFs when we set C_2H_6/C_2H_4 selectivity at 100 kPa and C_2H_6 uptake at 6.25 kPa (partial pressure of C_2H_6 in cracked gas mixtures) as concurrent objectives. The selectivity and C_2H_6 uptake in Tb-MOF-76(NH_2) are only lower than benchmark MAF-49 (2.7),[13a] $Fe_2(O_2)$(dobdc) (4.4),[7b] and ZJU-120a (2.74),[10] but higher than some top-performing C_2H_6-selective MOFs, such as MUF-15 (1.96),[20] Azole-Th-1 (1.46),[21] CPM-733 (1.75),[16] and ZIF-8 (1.7).[22] Taken together, previously reported C_2H_6-selective MOFs commonly display either low selectivity or few C_2H_6 uptake at low partial pressure, Tb-MOF-76(NH_2) exhibits a well balance in uptake and selectivity, rendering it among the benchmark material for this important separation.

To gain deeper insights into the origin of enhanced gas uptake and selectivity by $–NH_2$ functionalization, grand canonical Monte Carlo (GCMC) simulations were done to reveal the adsorption details. It shows that both C_2H_4 and C_2H_6 molecules are located at the corners of channels near

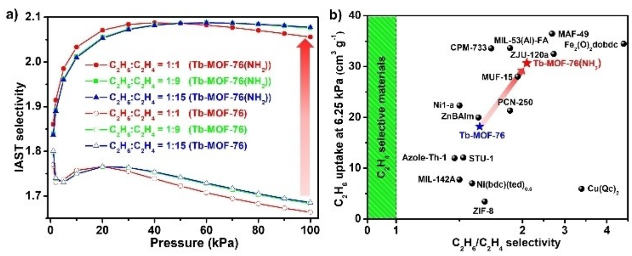

Figure 4. a) IAST selectivity of Tb-MOF-76 and Tb-MOF-76(NH_2) for C_2H_6/C_2H_4 mixtures; b) comparison of C_2H_6 uptakes and C_2H_6/C_2H_4 selectivity in different MOFs.

the rod-shaped SBUs. There only exists C–H⋯O hydrogen bonds between Tb-MOF-76 and C_2H_6 or C_2H_4 molecules, but for Tb-MOF-76(NH_2) there are not only C–H⋯O hydrogen bonds but also C–H⋯π and C–H⋯N interactions from the aromatic rings and –NH_2 groups of ligands. For Tb-MOF-76, the C_2H_6 molecule is bound to carboxyl O atoms from two BTC through four strong C–H⋯O interactions (H⋯O = 2.765–2.993 Å) (Figure 5a), by contrast, three weak C–H⋯O interactions (H⋯O distances = 3.165 Å–3.265 Å) formed with the C_2H_4 molecule are fewer and weaker (Figure 5b), in accord with the selectivity of C_2H_6 over C_2H_4. For Tb-MOF-76(NH_2), C_2H_6 interacts with one phenyl ring from the ligand, two amino N atoms and four O atoms from three carboxyl groups and one water ligand to form four C–H⋯O, two C–H⋯N, and one C–H⋯π interactions with the distances in the range of 2.681–3.082 Å (Figure 5c), but C_2H_4 forms weaker and fewer C–H⋯O/N/π interactions with longer distances (2.798–3.221 Å) (Figure 6d). As a result, the smaller pore sizes and more binding sites in Tb-MOF-76(NH_2) lead to C_2H_4 and C_2H_6 molecules in close contact with the pore walls compared to the corresponding gases with Tb-MOF-76. Meanwhile, it also reveals that in two MOFs there exist stronger contacts toward C_2H_6 than C_2H_4, agreeing with their C_2H_6-selective features.

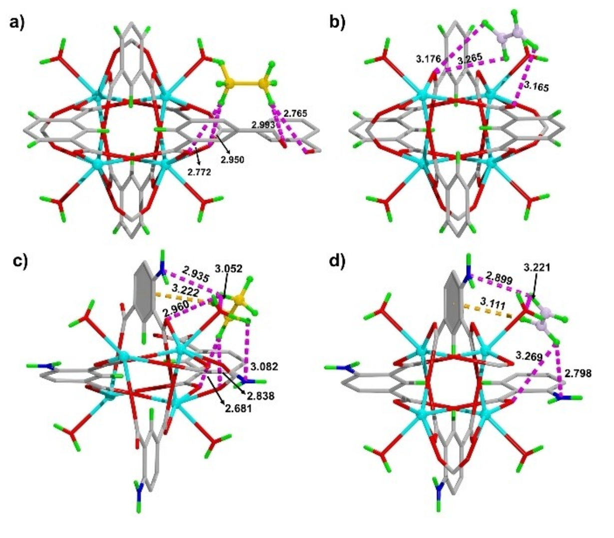

Figure 5. C_2H_6 and C_2H_4 preferential adsorption sites in Tb-MOF-76 (a and b) and Tb-MOF-76(NH_2) (c and d).

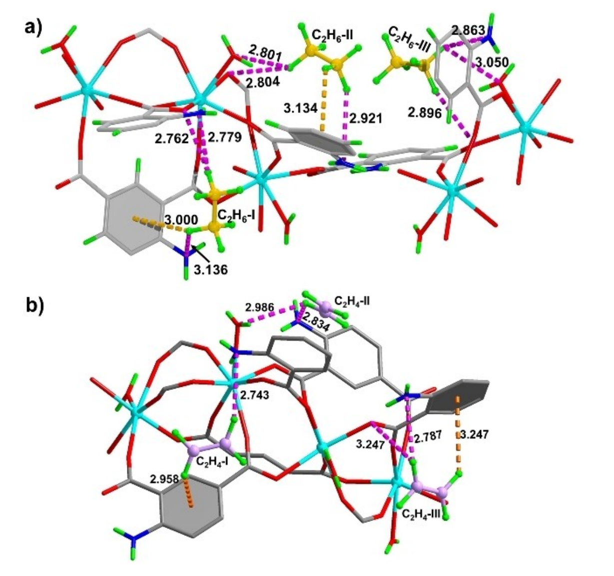

Figure 6. Adsorption sites of C_2H_6 (a) and C_2H_4 (b) in Tb-MOF-76(NH_2).

Furthermore, the interactions of C_2H_6 and C_2H_4 in Tb-MOF-76(NH_2) were further studied by simulations at 298 K and 100 kPa. It found three crucial C_2H_6 and C_2H_4 molecules interacting with the pore walls, as given in Figure 6. Both C_2H_6-I and C_2H_6-II form four strong C–H⋯π/N/O interactions with the phenyl groups, amino N atoms, and carboxyl O atoms, while C_2H_6-III interacts with carboxyl O and amino N atoms through three strong hydrogen bonds (Figure 6a). Three C_2H_4 molecules also contact with the framework through C–H⋯π/N/O hydrogen bonds (Figure 6b). In brief, there are more and stronger contacts between the framework and C_2H_6 compared to C_2H_4, thus forming a priority of adsorption for C_2H_6 over C_2H_4.

To validate the positive effect of –NH_2 groups on C_2H_6/C_2H_4 separation, transient breakthrough simulations for C_2H_6/C_2H_4 mixtures (1/1, 1/9, and 1/15, v/v) on Tb-MOF-76(NH_2) and Tb-MOF-76 in fixed beds were conducted at 298 K and 100 kPa (see Supporting Information).[22] As shown in Figure 7a,b,c, two MOFs can achieve efficient separations for three C_2H_6/C_2H_4 mixtures, wherein C_2H_4 breakthrough first occurred and subsequently reached a plateau to yield the polymer-grade C_2H_4, then C_2H_6 passed through the fixed bed after long times (τ_{break}). The separation potential (ΔQ) as a combined selectivity-capacity metric to quantify the mixture separation performance was utilized for further comparison.[7b,23] As given in Figure 7d,e,f, the amounts of pure C_2H_4 can be recovered by Tb-MOF-76(NH_2) reached up to 1.91, 4.61, and 4.95 mmol cm^{-3} for the 1/1, 1/9, and 1/15 mixtures, respectively, greatly outperform the values of 1.19, 2.65, and 2.82 mmol cm^{-3} in Tb-MOF-76. The ΔQ of Tb-MOF-76(NH_2) are not good as $Fe_2(O_2)$(dobdc),[7b] but are better than other C_2H_6-selective materials including MAF-49,[7b] UPC-613,[8d] PCN-250,[24] and UiO-67-$(NH_2)_2$,[8b] meaning the most promising prospect for C_2H_6/C_2H_4 separation (Table S3).

Next, dynamic breakthrough experiments were conducted at 298 K and 1 atm using C_2H_6/C_2H_4/Ar (5/5/90, 1/9/90, and 1/15/84, v/v/v) mixtures with Ar as the carrier gas introduced over the packed columns of Tb-MOF-76(NH_2) and MOF-76 (flow rate = 7.0 mL min^{-1}), respectively. The breakthrough curves depicted in Figure 8a,b,c show the effective separation of C_2H_6/C_2H_4 mixtures, in which Tb-MOF-76(NH_2) reveals an obviously better separation performance than Tb-MOF-76, in accordance with the single-component sorption, IAST selectivity, and transient breakthrough simulations. Comparing Figure 7a,b,c with Figure 8a,b,c, it is particularly noteworthy that the quantitative agreement between the transient breakthrough simulations with experiments. As predicted, C_2H_4 first eluted through

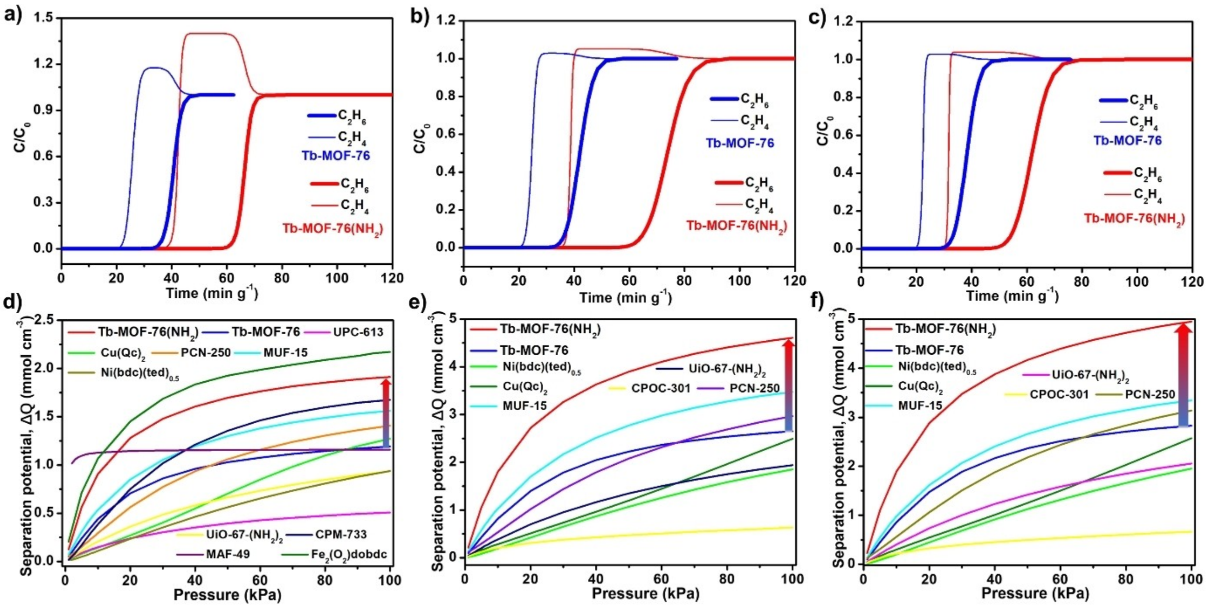

Figure 7. Simulated breakthrough curves of Tb-MOF-76(NH$_2$) and Tb-MOF-76 for C_2H_6/C_2H_4 mixtures: a) 1/1, b) 1/9, and c) 1/15; d–f) separation potential of selected MOFs for C_2H_6/C_2H_4 mixtures: d) 1/1, e) 1/9, and f) 1/15.

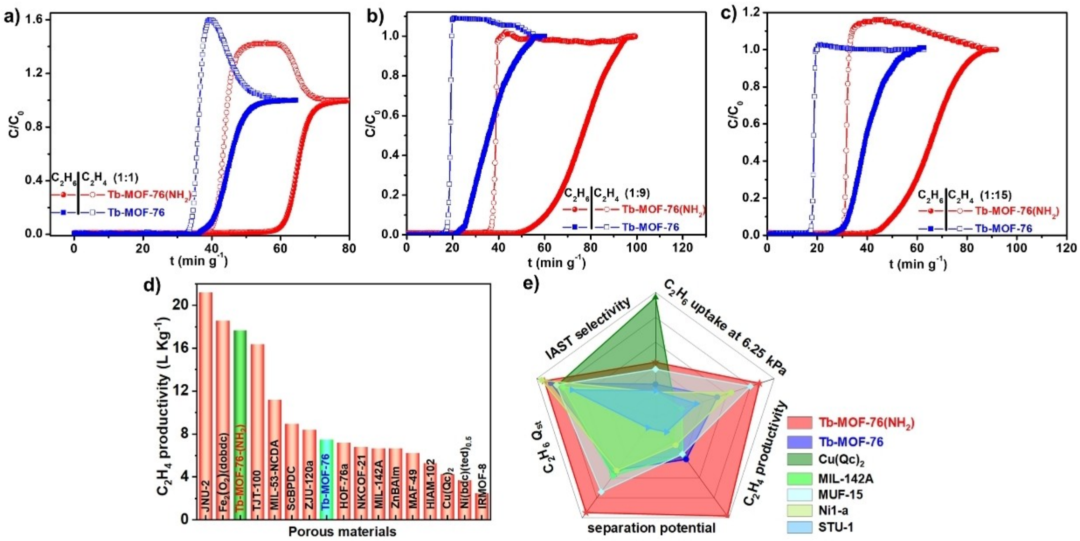

Figure 8. a–c) Experimental breakthrough curves of Tb-MOF-76(NH$_2$) and Tb-MOF-76 for C_2H_6/C_2H_4 mixtures at 298 K; d) comparison of C_2H_4 productivity for porous materials; e) comparison of the comprehensive separation performance in different C_2H_6-selective MOFs.

the column to yield an outflow of pure C_2H_4 (>99.9 %) with an undetectable C_2H_6 signal, whereas Tb-MOF-76(NH$_2$) retained C_2H_6 until reaching 58.5, 50.7, and 44.1 min g^{-1} for 1/1, 1/9, and 1/15 C_2H_6/C_2H_4 mixtures, respectively.

The productivities of ≥99.5 % and ≥99.95 % C_2H_4 purity were calculated on the basis of simulating experimental breakthrough curves to compare separation performance (Table S4). For Tb-MOF-76(NH$_2$), 6.20, 11.68, and 17.66 L kg^{-1} of C_2H_4 with ≥99.95 % purity can be recovered from the 1/1, 1/9, and 1/15 C_2H_6/C_2H_4 mixtures in one cycle; by contrast, the corresponding values of 1.90, 4.48, and 7.53 L kg^{-1} for Tb-MOF-76 are significantly lower. Notably, in industrial practice without containing inert carrier gas, the C_2H_4 productivity values for Tb-MOF-76(NH$_2$) would be higher than the found in our experiments. The value of 17.66 L kg^{-1} C_2H_4 (≥99.95 %) for Tb-MOF-76(NH$_2$) is nearly 2.4 times for Tb-MOF-76 with 7.53 L kg^{-1} (≥99.95 %), 2.5 times for HOF-76a with 7.2 L kg^{-1} (>99.9 %),[25] 2.8 times for MAF-49 with 6.27 L kg^{-1} (>99.95 %),[7b] 4 times for Cu(Qc)$_2$ with 4.4 L kg^{-1} (>99.9 %),[11] and only trails than top-performing JNU-2 with 21.1 L kg^{-1} (>99.99 %)[17] and Fe$_2$(O$_2$)(dobdc) with 18.59 L kg^{-1} (>99.95 %)[7b] (Figure 8d). For ≥99.5 % C_2H_4 purity, Tb-MOF-76(NH$_2$) also reveals obviously higher productivities than Tb-MOF-76 (Table S4). The higher separation potential and C_2H_4 productivity, determined from the breakthrough curves, confirm that the introduction of $-NH_2$ groups in the framework significantly improves the separation performance of MOFs for C_2H_6/C_2H_4 mixtures.

Great recyclability and reusability of adsorbents are essential conditions for practical industrial applications. For Tb-MOF-76(NH_2), we performed multiple breakthrough experiments of C_2H_6/C_2H_4 mixtures (1/1) under the same conditions, and it showed no any deterioration in separation performance (Figure S15). PXRD patterns also confirmed that the structural stability of Tb-MOF-76(NH_2) after cycle experiments (Figure S2 and S3). In a nutshell, Tb-MOF-76(NH_2) displays better one-step separation performance for C_2H_6/C_2H_4 mixtures than the reported C_2H_6-selective materials in references, in comprehensive consideration of separation potential, C_2H_4 productivity, C_2H_6/C_2H_4 selectivity, C_2H_6 uptake, and C_2H_6 Q_{st} (Figure 8e). These advances enable Tb-MOF-76(NH_2) to be one of excellent materials for C_2H_6/C_2H_4 separation.

Considering the real application environments, the stability of Tb-MOF-76(NH_2) toward air, water humidity, and acid-base environments was monitored by PXRD. As shown in Figure S16, after the samples were exposed in air for 40 days, relative humidity (65 %) for 10 days, and different aqueous solutions with pH = 3–10 for 1 day, it remains intact with no obvious phase transformation.

Conclusion

In summary, we have performed an uncommon and crucial systematic comparative example to tune the pore environment by pore engineering strategy using amino-functionalization for improving C_2H_6/C_2H_4 separation. The pore environments were successfully engineered by adopting the amino-functionalized linkers to replacing parent linkers in Tb-MOF-76. The obtained material Tb-MOF-76(NH_2) with the rich $-NH_2$ groups in pores displays significantly high C_2H_6 uptakes and C_2H_6/C_2H_4 adsorption selectivity compared to Tb-MOF-76 (2.1 *vs* 1.7). Consequently, Tb-MOF-76(NH_2) greatly improves the separation performance for C_2H_6/C_2H_4 mixtures, in which 17.66 $L\,kg^{-1}$ polymer-grade C_2H_4 product ($\geq$99.95 %) can be directly collected in a single breakthrough process compared to 7.53 $L\,kg^{-1}$ by Tb-MOF-76. Together with robust framework stability, Tb-MOF-76(NH_2) would be promising for the application in multiple separation process. The amino-functionalization method presented in this work is efficacious, and will provide an important strategy to facilitate the rational design of MOF adsorbents for efficient challenging industrial C_2H_6/C_2H_4 separation.

Acknowledgements

This work is supported by National Nature Science Foundation of China (21871220 and 21971207).

Conflict of Interest

The authors declare no conflict of interest.

Data Availability Statement

The data that support the findings of this study are available in the supplementary material of this article.

Keywords: Amino-Functionalization · C_2H_6/C_2H_4 Separation · Gas Adsorption · Metal–Organic Framework · Porous Engineering

[1] a) D. S. Sholl, R. P. Lively, *Nature* **2016**, *532*, 435–437; b) L. Zhang, L. Li, E. Hu, L. Yang, K. Shao, L. Yao, K. Jiang, Y. Cui, Y. Yang, B. Li, B. Chen, G. Qian, *Adv. Sci.* **2020**, *7*, 1901918.

[2] a) J.-R. Li, R. J. Kupplera, H.-C. Zhou, *Chem. Soc. Rev.* **2009**, *38*, 1477–1504; b) M. Kang, S. Yoon, S. Ga, D. W. Kang, S. Han, J. H. Choe, H. Kim, D. W. Kim, Y. G. Chung, C. S. Hong, *Adv. Sci.* **2021**, *8*, 2004940.

[3] a) H. Wang, D. Luo, E. Velasco, L. Yu, J. Li, *J. Mater. Chem. A* **2021**, *9*, 20874–20896; b) P.-D. Zhang, X. Zhang, X.-Q. Wu, Z.-C. Xu, J.-R. Li, *AIChE J.* **2022**, e17752; c) P. Hu, J. Hu, H. Wang, H. Liu, J. Zhou, Y. Liu, Y. Wang, H. Ji, *ACS Appl. Mater. Interfaces* **2022**, *14*, 15195–15204.

[4] S. Chu, Y. Cui, N. Liu, *Nat. Mater.* **2017**, *16*, 16–22.

[5] a) S. Zhou, O. Shekhah, A. Ramírez, P. Lyu, E. Abou-Hamad, J. Jia, J. Li, P. M. Bhatt, Z. Huang, H. Jiang, T. Jin, G. Maurin, J. Gascon, M. Eddaoudi, *Nature* **2022**, *606*, 706–712; b) H. Zeng, M. Xie, T. Wang, R.-J. Wei, X.-J. Xie, Y. Zhao, W. Lu, D. Li, *Nature* **2021**, *595*, 542–548; c) A. Cadiau, K. Adil, P. M. Bhatt, Y. Belmabkhout, M. Eddaoudi, *Science* **2016**, *353*, 137–140; d) P.-Q. Liao, N.-Y. Huang, W.-X. Zhang, J.-P. Zhang, X.-M. Chen, *Science* **2017**, *356*, 1193–1196; e) G.-D. Wang, Y.-Z. Li, W.-J. Shi, L. Hou, Y.-Y. Wang, Z. Zhu, *Angew. Chem. Int. Ed.* **2022**, *61*, e202205427; *Angew. Chem.* **2022**, *134*, e202205427.

[6] a) S. Mukherjee, D. Sensharma, K.-J. Chen, M. J. Zaworotko, *Chem. Commun.* **2020**, *56*, 10419–10441; b) S. Geng, E. Lin, X. Li, W. Liu, T. Wang, Z. Wang, D. Sensharma, S. Darwish, Y. H. Andaloussi, T. Pham, P. Cheng, M. J. Zaworotko, Y. Chen, Z. Zhang, *J. Am. Chem. Soc.* **2021**, *143*, 8654–8660.

[7] a) F. Jin, E. Lin, T. Wang, S. Geng, T. Wang, W. Liu, F. Xiong, Z. Wang, Y. Chen, P. Cheng, Z. Zhang, *J. Am. Chem. Soc.* **2022**, *144*, 5643–5652; b) L. Li, R.-B. Lin, R. Krishna, H. Li, S. Xiang, H. Wu, J. Li, W. Zhou, B. Chen, *Science* **2018**, *362*, 443–446.

[8] a) S.-Q. Yang, F.-Z. Sun, P. Liu, L. Li, R. Krishna, Y.-H. Zhang, Q. Li, L. Zhou, T.-L. Hu, *ACS Appl. Mater. Interfaces* **2021**, *13*, 962–969; b) X.-W. Gu, J.-X. Wang, E. Wu, H. Wu, W. Zhou, G. Qian, B. Chen, B. Li, *J. Am. Chem. Soc.* **2022**, *144*, 2614–2623; c) B. Zhu, J.-W. Cao, S. Mukherjee, T. Pham, T. Zhang, T. Wang, X. Jiang, K. A. Forrest, M. J. Zaworotko, K.-J. Chen, *J. Am. Chem. Soc.* **2021**, *143*, 1485–1492; d) Y. Wang, C. Hao, W. Fan, M. Fu, X. Wang, Z. Wang, L. Zhu, Y. Li, X. Lu, F. Dai, Z. Kang, R. Wang, W. Guo, S. Hu, D. Sun, *Angew. Chem. Int. Ed.* **2021**, *60*, 11350–11358; *Angew. Chem.* **2021**, *133*, 11451–11459; e) C.-X. Chen, Z.-W. Wei, T. Pham, P. C. Lan, L. Zhang, K. A. Forrest, S. Chen, A. M. Al-Enizi, A. Nafady, C.-Y. Su, S. Ma, *Angew. Chem. Int. Ed.* **2021**, *60*, 9680–9685; *Angew. Chem.* **2021**, *133*, 9766–9771.

[9] a) G.-D. Wang, J. Chen, Y.-Z. Li, L. Hou, Y.-Y. Wang, Z. Zhu, *Chem. Eng. J.* **2022**, *433*, 133786; b) Q. Hong, W. Wang, S. Chen, K. Chen, M. Liu, H.-X. Zhang, J. Zhang, *Chem. Mater.* **2022**, *34*, 307–313; c) K. H. Cho, J. W. Yoon, J. H. Lee, J. C. Kim, K. Kim, U.-H. Lee, M. Choi, S. K. Kwak, J.-S. Chang, *J. Mater. Chem. A* **2021**, *9*, 14593–14600; d) S. Jiang, L. Li, L. Guo, C. Song, Q. Yang, Z. Zhang, Y. Yang, Q. Ren, Z. Bao, *Sci. China Chem.* **2021**, *64*, 666–672; e) Y.-P. Li, Y.-N. Zhao, S.-N. Li, D.-Q. Yuan, Y.-C. Jiang, X. Bu, M.-C. Hu, Q.-G. Zhai, *Adv. Sci.* **2021**, *8*, 2003141.

[10] J. Pei, J.-X. Wang, K. Shao, Y. Yang, Y. Cui, H. Wu, W. Zhou, B. Li, G. Qian, *J. Mater. Chem. A* **2020**, *8*, 3613–3620.

[11] R.-B. Lin, H. Wu, L. Li, X.-L. Tang, Z. Li, J. Gao, H. Cui, W. Zhou, B. Chen, *J. Am. Chem. Soc.* **2018**, *140*, 12940–12946.

[12] a) B. Arstad, H. Fjellvåg, K. O. Kongshaug, O. Swang, R. Blom, *Adsorption* **2008**, *14*, 755–762; b) X. Zhang, R. B. Lin, H. Wu, Y. Huang, Y. Ye, J. Duan, W. Zhou, J.-R. Li, B. Chen, *Chem. Eng. J.* **2022**, *431*, 134184; c) S. Couck, J. F. M. Denayer, G. V. Baron, T. Rémy, J. Gascon, F. Kapteijn, *J. Am. Chem. Soc.* **2009**, *131*, 6326–6327; d) Kalmutzki, R. M. Altamimi, F. Fathieh, J. A. Reimer, O. M. Yaghi, *J. Am. Chem. Soc.* **2017**, *139*, 12125–12128; e) B. Dinakar, A. C. Forse, H. Z. H. Jiang, Z. Zhu, J.-H. Lee, E. J. Kim, S. T. Parker, C. J. Pollak, R. L. Siegelman, P. J. Milner, J. A. Reimer, J. R. Long, *J. Am. Chem. Soc.* **2021**, *143*, 15258–15270; f) E. J. Kim, R. L. Siegelman, H. Z. H. Jiang, A. C. Forse, J.-H. Lee, J. D. Martell, P. J. Milner, J. M. Falkowski, J. B. Neaton, J. A. Reimer, S. C. Weston, J. R. Long, *Science* **2020**, *369*, 392–396.

[13] a) P.-Q. Liao, W.-X. Zhang, J.-P. Zhang, X.-M. Chen, *Nat. Commun.* **2015**, *6*, 8697; b) T.-L. Hu, H. Wang, B. Li, R. Krishna, H. Wu, W. Zhou, Y. Zhao, Y. Han, X. Wang, W. Zhu, Z. Yao, S. Xiang, B. Chen, *Nat. Commun.* **2015**, *6*, 7328.

[14] C. He, Y. Wang, Y. Chen, X. Wang, J. Yang, L. Li, J. Li, *Ind. Eng. Chem. Res.* **2020**, *59*, 6123–6129.

[15] Deposition Number 2192249 contains the supplementary crystallographic data for this paper. These data are provided free of charge by the joint Cambridge Crystallographic Data Centre and Fachinformationszentrum Karlsruhe Access Structures service.

[16] H. Yang, Y. Wang, R. Krishna, X. Jia, Y. Wang, A. N. Hong, C. Dang, H. E. Castillo, X. Bu, P. Feng, *J. Am. Chem. Soc.* **2020**, *142*, 2222–2227.

[17] H. Zeng, X.-J. Xie, M. Xie, Y.-L. Huang, D. Luo, T. Wang, Y. Zhao, W. Lu, D. Li, *J. Am. Chem. Soc.* **2019**, *141*, 20390–20396.

[18] H.-G. Hao, Y.-F. Zhao, D.-M. Chen, J.-M. Yu, K. Tan, S. Ma, Y. Chabal, Z.-M. Zhang, J.-M. Dou, Z.-H. Xiao, G. Day, H.-C. Zhou, T.-B. Lu, *Angew. Chem. Int. Ed.* **2018**, *57*, 16067–16071; *Angew. Chem.* **2018**, *130*, 16299–16303.

[19] J. Liu, J. Miao, S. Ullah, K. Zhou, L. Yu, H. Wang, Y. Wang, T. Thonhauser, J. Li, *ACS Mater. Lett.* **2022**, *4*, 1227–1232.

[20] O. T. Qazvini, R. Babarao, Z.-L. Shi, Y.-B. Zhang, S. G. Telfer, *J. Am. Chem. Soc.* **2019**, *141*, 5014–5020.

[21] Z. Xu, X. Xiong, J. Xiong, R. Krishna, L. Li, Y. Fan, F. Luo, B. Chen, *Nat. Commun.* **2020**, *11*, 3163.

[22] U. Böhme, B. Barth, C. Paula, A. Kuhnt, W. Schwieger, A. Mundstock, J. Caro, M. Hartmann, *Langmuir* **2013**, *29*, 8592–8600.

[23] a) R. Krishna, *RSC Adv.* **2017**, *7*, 35724–35737; b) R. Krishna, *ACS Omega* **2020**, *5*, 16987–17004.

[24] Y. Chen, Z. Qiao, H. Wu, D. Lv, R. Shi, Q. Xia, J. Zhou, Z. Li, *Chem. Eng. Sci.* **2018**, *175*, 110–117.

[25] X. Zhang, L. Li, J.-X. Wang, H.-M. Wen, R. Krishna, H. Wu, W. Zhou, Z.-N. Chen, B. Li, G. Qian, B. Chen, *J. Am. Chem. Soc.* **2020**, *142*, 633–640.

Manuscript received: September 4, 2022
Accepted manuscript online: October 6, 2022
Version of record online: October 26, 2022

Angewandte Chemie
Eine Zeitschrift der Gesellschaft Deutscher Chemiker

Supporting Information

Boosting Ethane/Ethylene Separation by MOFs through the Amino-Functionalization of Pores

G.-D. Wang, R. Krishna, Y.-Z. Li, W.-J. Shi, L. Hou, Y.-Y. Wang, Z. Zhu*

Table of Contents

Materials and general methods

The chemicals were purchased commercially from Adamas-beta. Elemental analyses of C, H, and N were determined with a Perkin-Elmer 2400C elemental analyzer. Thermalgravimetric analyses (TGA) were carried out in a nitrogen stream using a Netzsch TG209F3 equipment at a heating rate of 10 °C min^{-1}. Single crystal diffraction data were collected on a Bruker SMART APEX II CCD single crystal diffractometer (Supporting Information). Gas adsorption curves were collected with Micromeritics ASAP 2020M and TriStar II 3020 equipments. Breakthrough experiments were performed on a Quantachrome dynaSorb BT equipment.

Synthesis of MOFs

Synthesis of Tb-MOF-76.

Tb-MOF-76 was synthesized according to reported literature procedure with slight modification.[1] In a typical process, $Tb(NO_3)\cdot 6H_2O$ (0.0456 g), 1,3,5-benzenetricarboxylate (BTC) (0.021 g), N,N-dimethylformamide (DMF) (4 mL), and H_2O (4 mL) were placed in a 15 mL Teflon-lined reactor. The mixture was heated at 105 °C for 72 h and slowly cooled to room temperature. Needle-like crystals of MOF-76 were collected by filtration.

Synthesis of Tb-MOF-76(NH_2).

In a typical process, $Tb(NO_3)\cdot 6H_2O$ (0.0456 g), 1,3,5-benzenetricarboxylate-NH_2 (BTC-NH_2) (0.022 g), N-Methylformamide (NMF) (3 mL), CH_3CN (0.5 mL), H_2O (0.5 mL) and HCl (0.5 mL) were placed in a 15 mL Teflon-lined reactor. The mixture was heated at 130 °C for 72 h and slowly cooled to room temperature. Needle-like crystals of MOF-76(NH_2) were collected by filtration.

Powder X-ray diffraction (PXRD)

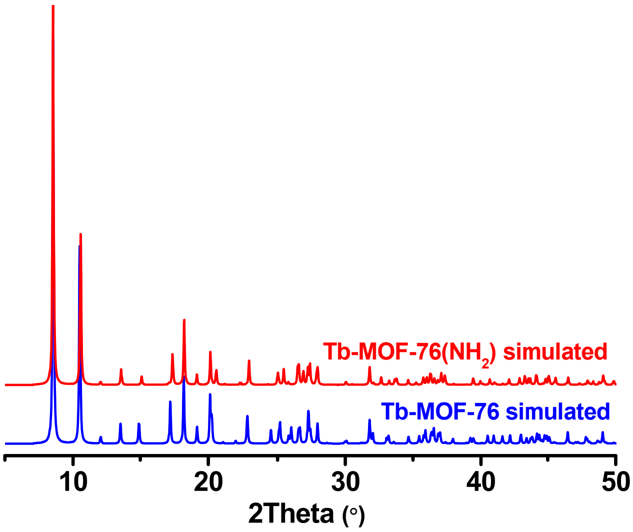

Figure S1. The PXRD patterns of as-synthesized Tb-MOF-76 (blue) and Tb-MOF-76(NH_2) (red), indicating their same structure.

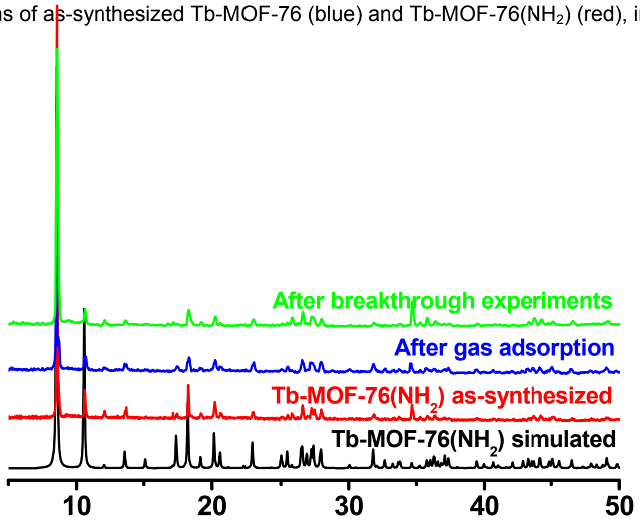

Figure S2. The calculated PXRD pattern from the crystal structure of Tb-MOF-76(NH_2) (black) and PXRD patterns of as-synthesized Tb-MOF-76(NH_2) (red), after gas adsorption samples (blue) and after breakthrough experiments (green).

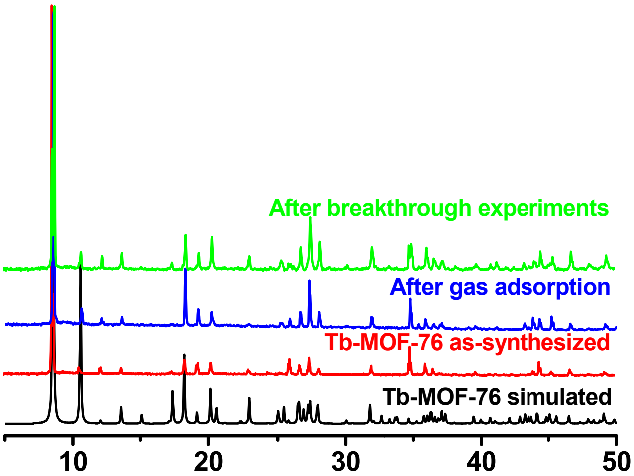

Figure S3. The calculated PXRD pattern from the crystal structure of Tb-MOF-76 (black) and PXRD patterns of as-synthesized Tb-MOF-76 (red), after gas adsorption samples (blue) and after breakthrough experiments (green).

X-ray crystallography

A Bruker Smart Apex II CCD detector was used to collect the single crystal data of Tb-MOF-76(NH_2) at 180(2) K using Mo Kα radiation (λ = 0.71073 Å). The structure was solved by direct methods and refined by full-matrix least-squares refinement based on F^2 with the SHELXTL program.The non-hydrogen atoms were refined anisotropically with the hydrogen atoms added at their geometrically ideal positions and refined isotropically. As the disordered solvent molecules in the structure cannot be located, the SQUEEZE routine of Platon program was applied in refining. The formula of complex was get by the single crystal analysis together with elemental microanalyses and TGA data. Relevant crystallographic results are listed in Table S1. Selected bond lengths and angles are provided in Table S2.

Table S1. Crystallographic data for Tb-MOF-76(NH_2) and Tb-MOF-76.[1]

Chemical formula	$C_9H_6TbNO_7$	$C_9H_5TbO_7$
Formula weight	399.07	384.05
T (K)	180(2) K	-----
Crystal system, Space group	Tetragonal, $P4_122$	Tetragonal, $P4_322$
a (Å), b (Å), c (Å)	10.3464(3)	10.3300(15)
b (Å)	10.3464(3)	10.3300(15)
c (Å)	14.2185(8)	14.510(3)
α (°), β (°), γ (°)	90,90,90	90,90,90
V (Å^3)	1522.06(12)	1548.3(4)
Z, $D_{calcd.}$[g·cm^{-3}]	4, 1.742	4, 1.639
μ (mm^{-1}), Goof	4.666, 1.095	4.581, 1.096
Reflns collected/unique/R_{int}	13955/ 1402/ 0.0326	15015/ 1768/ 0.0468
$R_1{}^a$, $wR_2{}^b$ [I > 2σ]	0.0208, 0.0517	0.0188, 0.0453
$R_1{}^a$, $wR_2{}^b$ (all data)	0.0215, 0.0521	0.0210, 0.0458

$^aR_1 = \Sigma(|F_o|-|F_c|)/\Sigma|F_o|$. $^bR_2 = [\Sigma w(F_o^2 - F_c^2)^2/\Sigma w(F_o^2)^2]^{1/2}$.

Table S2. Selected bond lengths (Å) and bond angles (deg) for Tb-MOF-76(NH_2).

Tb(1)-O(1)	2.287(5)	O(1)-Tb(1)-O(2)#4	147.3(2)
Tb(1)-O(1)#1	2.287(5)	O(1)#1-Tb(1)-O(2)#4	75.2(2)
Tb(1)-O(3)#2	2.298(5)	O(3)#2-Tb(1)-O(2)#4	105.3(3)
Tb(1)-O(3)#3	2.298(5)	O(3)#3-Tb(1)-O(2)#4	92.3(3)
Tb(1)-O(2)#4	2.324(6)	O(1)-Tb(1)-O(2)#5	75.2(2)
Tb(1)-O(2)#5	2.324(6)	O(1)#1-Tb(1)-O(2)#5	147.3(2)
Tb(1)-O(1W)	2.501(14)	O(3)#2-Tb(1)-O(2)#5	92.3(3)
O(2)-Tb(1)#7	2.324(6)	O(3)#3-Tb(1)-O(2)#5	105.3(3)
O(3)-Tb(1)#8	2.298(5)	O(2)#4-Tb(1)-O(2)#5	72.1(3)
O(1)-Tb(1)-O(1)#1	137.4(3)	O(1)-Tb(1)-O(1W)	68.72(17)
O(1)-Tb(1)-O(3)#2	77.7(2)	O(1)#1-Tb(1)-O(1W)	68.72(17)
O(1)#1-Tb(1)-O(3)#2	94.4(2)	O(3)#2-Tb(1)-O(1W)	79.2(2)
O(1)-Tb(1)-O(3)#3	94.4(2)	O(3)#3-Tb(1)-O(1W)	79.2(2)
O(1)#1-Tb(1)-O(3)#3	77.7(2)	O(2)#4-Tb(1)-O(1W)	143.93(16)
O(3)#2-Tb(1)-O(3)#3	158.3(4)	O(2)#5-Tb(1)-O(1W)	143.93(16)

Symmetry codes: #1 -y+1,-x+1,-z+1/4; #2 x,-y+2,-z+1/2; #3 y-1,-x+1,z-1/4; #4 x,y-1,z; #5 -y+2,-x+1,-z+1/4.

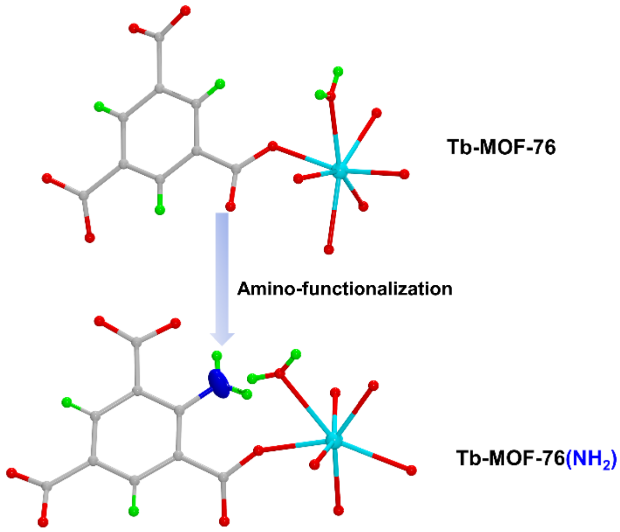

Figure S4. Coordination environments of Tb^{3+} ions in Tb-MOF-76 and Tb-MOF-76(NH_2).

Thermogravimetric analysis (TGA)

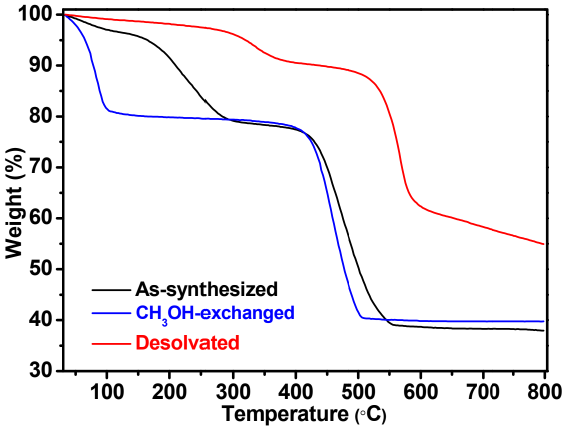

Figure S5. TGA curves of as-synthesized, CH_3OH-exchanged, and desolvated samples of Tb-MOF-76(NH_2).

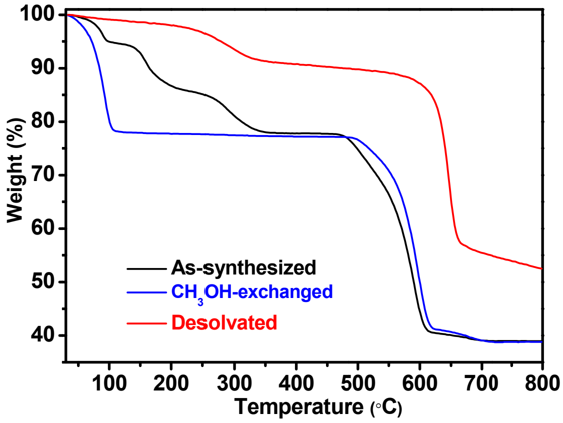

Figure S6. TGA curves of as-synthesized, CH_3OH-exchanged, and desolvated samples of Tb-MOF-76.

Fitting adsorption heat of pure component isotherms

$$\ln P = \ln N + 1/T\sum_{i=0}^{m} a_i N^i + \sum_{i=0}^{n} b_i N^i \qquad Q_{st} = -R\sum_{i=0}^{m} a_i N^i$$

The above virial expression was used to fit the combined isotherm data of the MOFs at 273, 298, and 313 K, where P is the pressure, N is the adsorbed amount, T is the temperature, a_i and b_i are virial coefficients, and m and N are the number of coefficients used to describe the isotherms. Q_{st} is the coverage-dependent enthalpy of adsorption and R is the universal gas constant.

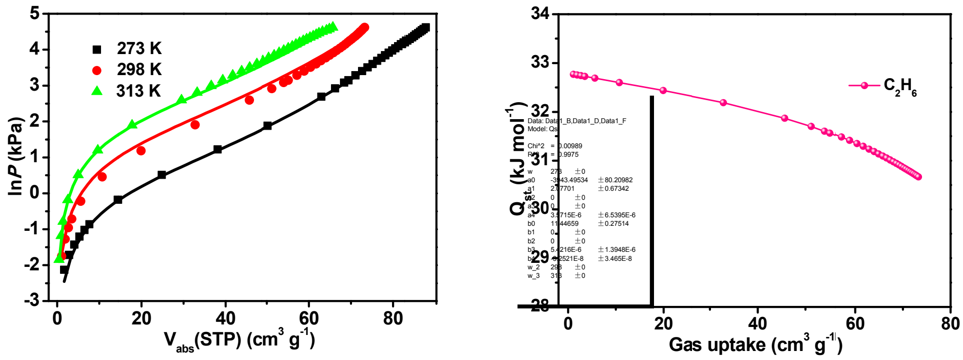

Figure S7. Fitted C_2H_6 isotherms of Tb-MOF-76(NH$_2$), and the isosteric heats of adsorption (Q_{st}). Fitting results, a0 = -3943.49534, a1 = 2.07701, a4 = 3.5715E-6, b0 = 11.44659, b3 = 5.4216E-6, b4 = -3.2521E-8, Chi^2 = 0.00989, R^2 = 0.9975.

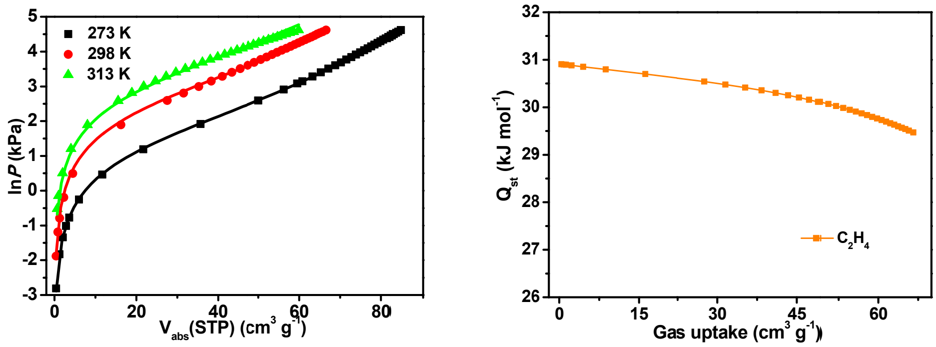

Figure S8. Fitted C_2H_4 isotherms of Tb-MOF-76(NH$_2$), and the isosteric heats of adsorption (Q_{st}). Fitting results, a0 = -3717.7822, a1 = 1.52923, a4 = 3.639E-6, b0 = 11.55632, b2 = 0.00016, Chi^2 = 0.00369, R^2 = 0.99891.

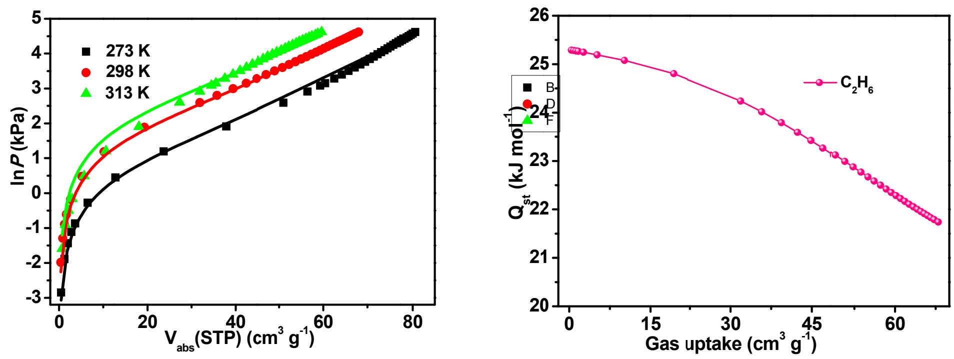

Figure S9. Fitted C_2H_6 isotherms of Tb-MOF-76, and the isosteric heats of adsorption (Q_{st}). Fitting results, a0 = -3042.87311, a1 = 2.41366, a3 = 0.0022, a4 = -0.00002, b0 = 8.85515, Chi^2 = 0.02077, R^2 = 0.9946.

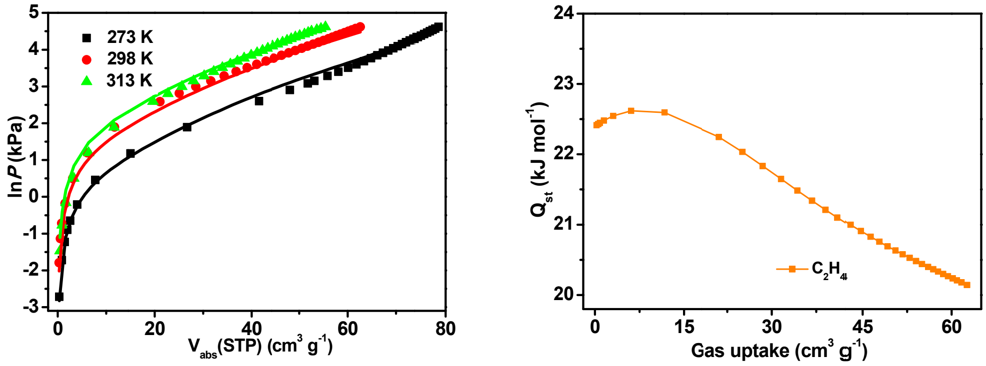

Figure S10. Fitted C_2H_4 isotherms of Tb-MOF-76, and the isosteric heats of adsorption (Q_{st}). Fitting results, a0 = -2693.8611, a1 = -7.49522, a2 = 0.56767, a3 = -0.00918, a4 = 0.00005, b0 = 8.31135, Chi^2 = 0.01658, R^2 = 0.99532.

Gas adsorption isotherm

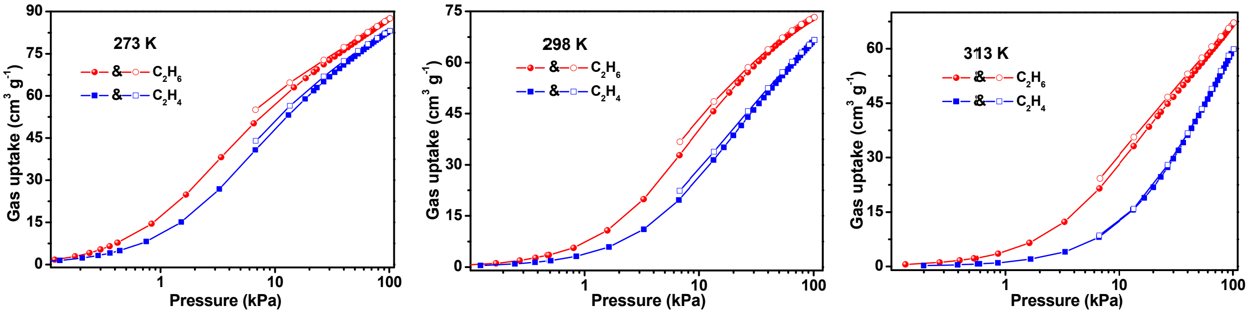

Figure S11. Gas adsorption isotherms of Tb-MOF-76(NH$_2$) for C_2H_6 and C_2H_4 at 273, 298, and 313 K.

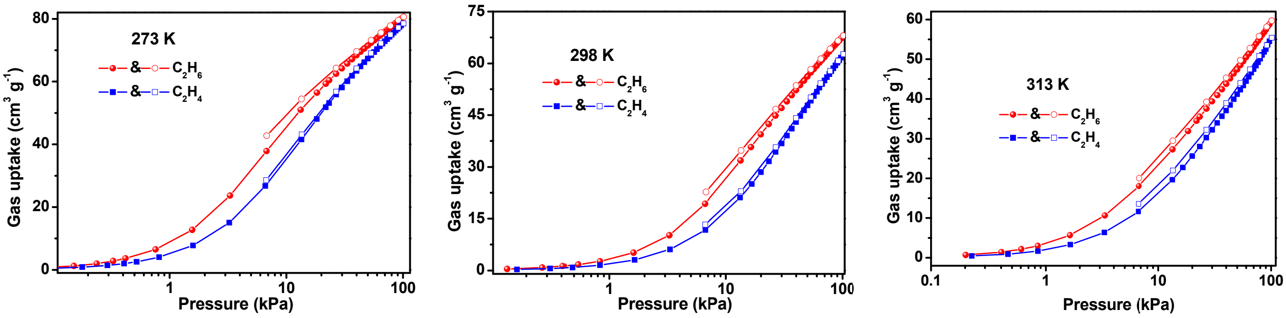

Figure S12. Gas adsorption isotherms of Tb-MOF-76 for C_2H_6 and C_2H_4 at 273, 298, and 313 K.

Gas selectivity prediction via IAST

The experimental isotherm data for pure C_2H_4 and C_2H_6 were fitted using a dual Langmuir-Freundlich (L-F) model:

$$q = \frac{a_1 * b_1 * P^{c_1}}{1 + b_1 * P^{c_1}} + \frac{a_2 * b_2 * P^{c_2}}{1 + b_2 * P^{c_2}}$$

Where *q* and *p* are adsorbed amounts and the pressure of component i, respectively.

The adsorption selectivities for binary mixtures defined by

$$S_{i/j} = \frac{x_i * y_j}{x_j * y_i}$$

were respectively calculated using the Ideal Adsorption Solution Theory (IAST). Where x_i is the mole fraction of component *i* in the adsorbed phase and y_i is the mole fraction of component i in the bulk.

Besides adsorption selectivities, a combined selectivity-capacity metric, called the separation potential, ΔQ, was firstly introduced by Rajamani Krishna[2,3] to reflects mixture separations capability of the MOF. For a C_2H_6/C_2H_4 mixture with mole fractions yC_2H_6, and $yC_2H_6=1-yC_2H_4$, ΔQ is calculated from IAST using the formula

$$\Delta Q = \left(q_{C2H6}\frac{yC2H4}{yC2H6} - q_{C2H4}\right)\rho$$

where ρ is the crystal framework density of the MOF, expressed say in units of kg m^{-3}, or g cm^{-3}.

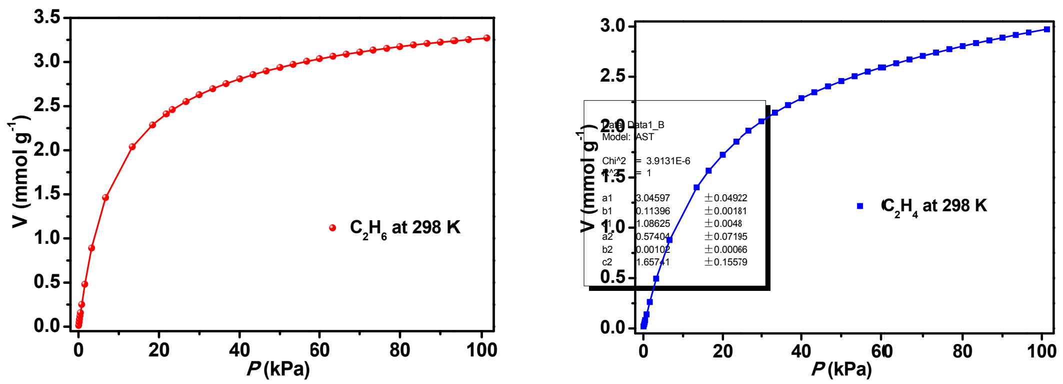

Figure S13. C_2H_6 and C_2H_4 adsorption isotherms of Tb-MOF-76(NH_2) with fitted by dual L-F model at 298 K, C_2H_6: a1 = 3.04597, b1 = 0.11396, c1 = 1.08625, a2 = 0.57404, b2 = 0.00102, c2 = 1.65741, Chi^2 = 3.9131E-6, R^2 = 1; C_2H_4: a1 = 2.96235, b1 = 0.05795, c1 = 1.04013, a2 = 1.1687, b2 = 0.00053, c2 = 1.47522, Chi^2 = 7.4485E-7, R^2 = 1.

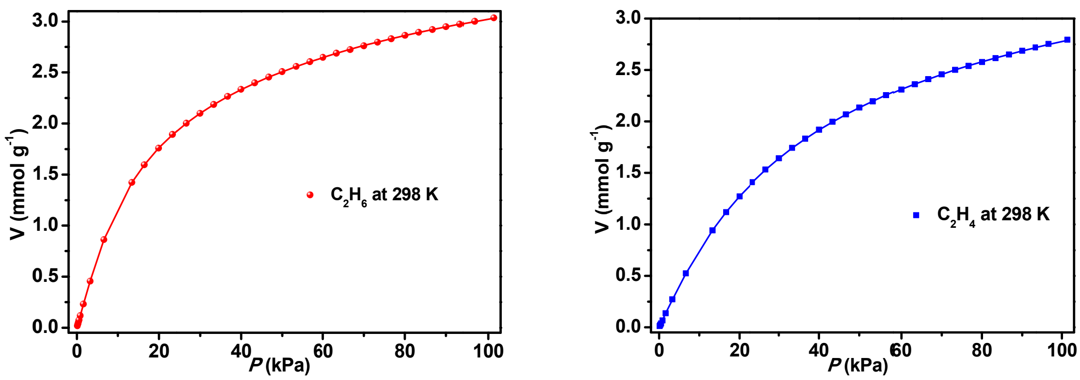

Figure S14. C_2H_6 and C_2H_4 adsorption isotherms of Tb-MOF-76 with fitted by dual L-F model at 298 K, C_2H_6: a1 = 3.17612, b1 = 0.02884, c1 = 0.81281, a2 = 1.32366, b2 = 0.03956, c2 = 1.42285, Chi^2 = 4.6915E-6, R^2 = 1; C_2H_4: a1 = 3.88323, b1 = 0.02166, c1 = 0.98921, a2 = 0.16476, b2 = 0.00768, c2 = 2.00594, Chi^2 = 6.713E-6, R^2 = 0.99999.

Molecular simulations

Grand canonical Monte Carlo (GCMC) simulations were performed for the gas adsorption in the framework by the Sorption module of Material Studio (Accelrys. Materials Studio Getting Started). The framework was considered to be rigid, and the optimized gas molecules were used. The partial charges for atoms of the framework were derived from QEq method and QEq neutral 1.0 parameter. One unit cell was used during the simulations. The interaction energies between the gas molecules and framework were computed through the Coulomb and Lennard-Jones 6-12 (LJ) potentials. All parameters for the atoms were modeled with the universal force field (UFF) embedded in the MS modeling package. A cutoff distance of 12.5 Å was used for LJ interactions, and the Coulombic interactions were calculated by using Ewald summation. For each run, the 3×10^6 maximum loading steps, 3×10^6 production steps were employed.

Transient breakthrough simulations

Transient breakthrough simulations were carried out for the same set of operating conditions as in the experimental data sets, packed sample weight, w = 0.8 g; length of packed bed, L = 8 cm; diameter of packed bed, d = 0.42 cm; the gas mixtures contain C_2H_6/C_2H_4/Ar (5/5/90, 1/9/90, and 1/15/84, v/v/v) with Ar as the carrier gas, and a total flow rate of 7.0 mL min^{-1} (298 K, 1 atm). using the methodology described in earlier publications.[S2-6] In these simulations, intra-crystalline diffusion influences are ignored. For Tb-MOF-76(NH_2), there is excellent match between the experiments and simulations. From the simulations on the experimental breakthrough curves, the productivities of ≥99.95% and ≥99.5% pure C_2H_4 were determined, which are expressed in the units of L per kg of MOF.

Breakthrough experiment

The breakthrough experiment was performed on the Quantachrome dynaSorb BT equipments at 298 K and 100 kPa with different ratios of mixed gas (C_2H_6/C_2H_4/Ar = 5/5/90, 1/9/90, and 1/15/84, v/v/v, Ar as the carrier gas, flow rate = 7 mL min^{-1}). The activated Tb-MOF-76(NH_2) and Tb-MOF-76 (about 0.8 g) was filled into a packed column of ϕ 4.2×80 mm, and then the packed column was washed with Ar at a rate of 7 mL min^{-1} at 343 K for 30 minutes to further activate the samples. Between two breakthrough experiments, the adsorbent was regenerated by Ar flow of 7 mL min^{-1} for 35 min at 343 K to guarantee a complete removal of the adsorbed gas.

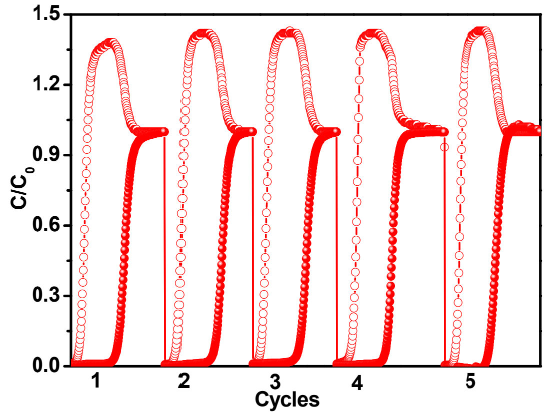

Figure S15. Five cycles of breakthrough curves of Tb-MOF-76(NH_2) for equimolar C_2H_6/C_2H_4 mixtures at 298 K.

Stability test

To investigate the chemical stabilities of Tb-MOF-76(NH_2), the as-synthesized samples were soaked in water, HCl (pH = 3) and NaOH (pH = 10) solutions for 1 day, exposed to air for 40 days and 65 humidity for 10 days, respectively. And then characterized by PXRD measurements in order to determine whether the sample retains its structural integrity.

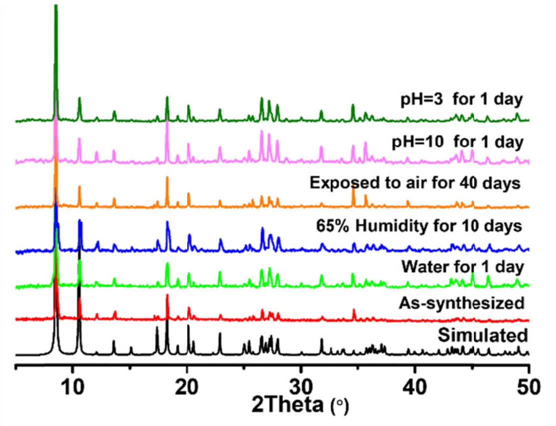

Figure S16. PXRD patterns of Tb-MOF-76(NH_2) treated under different conditions.

Screening result for some high-performance C_2H_6 MOF adsorbents

Table S3. Comparison of separation potential ΔQ for C_2H_6/C_2H_4 mixture of different adsorbents

Separation potential ΔQ mmol cm^{-3}					
Adsorbents	C_2H_6/C_2H_4 (1/1,v/v)	C_2H_6/C_2H_4 (1/9,v/v)	C_2H_6/C_2H_4 (1/15,v/v)	Crystal density (g cm^{-3})	Ref.
Tb-MOF-76(NH_2)	1.91	4.61	4.95	1.742	This work
Tb-MOF-76	1.19	2.65	2.82	1.639	This work
Ni(bdc)(ted)$_{0.5}$	0.94	1.85	1.95	0.830	7
Cu(Qc)$_2$	1.27	2.49	2.57	1.492	8
PCN-250	1.41	2.96	3.13	0.957	9
MUF-15	1.56	3.47	3.70	1.245	10
$Fe_2(O_2)$dobdc	2.17	--	--	1.255	11
UPC-613	0.51	--	--	1.115	12
UiO-67-(NH_2)$_2$	0.94	1.94	2.06	0.819	13
MAF-49	1.16	--	--	1.481	14
CPM-733	1.67	--	--	0.890	15

Table S4. Comparisons of C_2H_4 productivities of Tb-MOF-76(NH_2) and Tb-MOF-76 in experimental breakthrough curves using C_2H_6/C_2H_4 mixture as input.

		Gravimetric productivity (L Kg^{-1}) with different purities of C_2H_4	
MOFs		≥99.5%	≥99.95%
Tb-MOF-76(NH_2)	C_2H_6/C_2H_4 (1/1,v/v)	7.53	6.20
	C_2H_6/C_2H_4 (1/9,v/v)	14.99	11.68
	C_2H_6/C_2H_4 (1/15,v/v)	22.66	17.66
Tb-MOF-76	C_2H_6/C_2H_4 (1/1,v/v)	2.88	1.90
	C_2H_6/C_2H_4 (1/9,v/v)	6.53	4.48
	C_2H_6/C_2H_4 (1/15,v/v)	10.77	7.53

References

[1] H.-L. Jiang, N. Tsumori and Q. Xu, *Inorg. Chem.* **2010**, 49, 10001-10006.
[2] R. Krishna, *RSC Adv*. **2017**, 7, 35724-35737.
[3] R. Krishna, *ACS Omega* **2020**, 5, 16987−17004.
[4] R. Krishna, *RSC Adv*. **2015**, 5, 52269-52295.
[5] R. Krishna, *Microporous Mesoporous Mater*. **2014**, 185, 30-50.
[6] R. Krishna, *Sep. Purif. Technol*. **2018**, 194, 281-300.
[7] W. Liang, F. Xu, X. Zhou, J. Xiao, Q. Xia, Y. Li, Z. Li, *Chem. Eng. Sci*. **2016**, 148, 275-281.
[8] R.-B. Lin, H. Wu, L. Li, X.-L. Tang, Z. Li, J. Gao, H. Cui, W. Zhou and B. Chen, *J. Am. Chem. Soc.* **2018**, 140, 12940-12946.
[9] Y. Chen, Z. Qiao, H. Wu, D. Lv, R. Shi, Q. Xia, J. Zhou, Z. Li, *Chem. Eng. Sci*. **2018**, 175, 110-117.
[10] O. T. Qazvini, R. Babarao, Z.-L. Shi, Y.-B. Zhang and S. G. Telfer, *J. Am. Chem. Soc.* **2019**, 141, 5014-5020.
[11] L. Li, R.-B. Lin, R. Krishna, H. Li, S. Xiang, H. Wu, J. Li, W Zhou, B. Chen, *Science* **2018**, 362, 443-446.
[12] Y. Wang, C. Hao, W. Fan, M. Fu, X. Wang, Z. Wang, L. Zhu, Y. Li, X. Lu, F. Dai, Z. Kang, R. Wang, W. Guo, S. Hu and D. Sun, *Angew. Chem. Int. Ed.* **2021**, 60, 11350-11358.
[13] X.-W. Gu, J.-X. Wang, E. Wu, H. Wu, W. Zhou, G. Qian, B. Chen and B. Li, *J. Am. Chem. Soc.* **2022**, 144, 2614–2623.
[14] P.-Q. Liao, W.-X. Zhang, J.-P. Zhang, X,-M, Chen, *Nat. Com*. **2015**, 6, 8697.
[15] H. Yang, Y. Wang, R. Krishna, X. Jia, Y. Wang, A. N. Hong, C. Dang, H. E. Castillo, X. Bu and P. Feng, *J. Am. Chem. Soc.* **2020**, 142, 2222−2227.

Author contributions

Gang-Ding Wang: Experimental, Writing - original draft. **Rajamani Krishna:** Formal analysis, Software. **Yong-Zhi Li:** Formal analysis, Writing - review & editing. **Wen-Juan Shi:** Formal analysis, Software. **Lei Hou:** Software, Writing - review & editing, Supervision, Funding acquisition. **Yao-Yu Wang:** Formal analysis, Resources. **Zhonghua Zhu:** Formal analysis.